Energy & Environmental Science

ROYAL SOCIETY OF CHEMISTRY

PAPER

View Article Online
View Journal | View Issue

Cite this: *Energy Environ. Sci.*, 2024, **17**, 8745

Water-induced spinodal decomposition of mixed halide perovskite captured by real-time liquid TEM imaging†

Nicolas Folastre,[ab] Mohammad Ali Akhavan Kazemi,[a] Kirill Cherednichneko,[ab] Arash Jamali,[c] Jean Rousset,[de] Frédéric Sauvage *[a] and Arnaud Demortière[ab]

Received 29th July 2024,
Accepted 23rd September 2024

DOI: 10.1039/d4ee03381g

rsc.li/ees

Hybrid halide perovskite materials face significant challenges in reaching long-term stability, particularly due to their vulnerability to humidity. While encapsulation can provide some protection by delaying the water-induced degradation, understanding the precise reaction pathways is crucial for developing more robust compositions and advanced device architectures. Traditional *ex situ* methods offer only snapshots of degradation states, failing to capture the initiation and full evolution of the degradation process in real time. In this study, we utilize cutting-edge real-time electron imaging and *in situ* liquid-cell transmission electron microscopy to dynamically observe the degradation processes of the $Cs_{0.05}(MA_{0.17}FA_{0.83})_{0.95}Pb(Br_{0.17}I_{0.83})_3$ (CsMAFA) perovskite in contact with water molecules. Using *in situ* live TEM imaging, combined to SAED and 4D-STEM ACOM techniques, we capture the subsequent degradation steps at both nanoscopic and mesoscopic levels from inception to full degradation. Our results particularly support the spinodal nature of the early-stage decomposition of the perovskite, where a spontaneous coexistence of CsMAFA, PbI_2 and $CsPb_2Br_5$ is observed within a single grain upon contact with water molecules. This step either competes with, or, is followed by a dissolution/recrystallization mechanism from CsMAFA to PbI_2 grains, while the solid-state spinodal decomposition of CsMAFA to $CsPb_2Br_5$ continues. From live image segmentations, two different growth rates of PbI_2 are highlighted, *i.e.* in $t^{1/2}$ and $t^{1/3}$, controlling the final particles morphology into fine polygons and needles. Longer exposure times leads to two stages, firstly the complete degradation of the pristine perovskite, resulting in the two end members, namely PbI_2 and $CsPb_2Br_5$ as a single-phase particles, secondly the dissolution of the $CsPb_2Br_5$ particles and disentangling of the remaining PbI_2 particles.

Broader context

Halide perovskite materials have significant potential to revolutionize various fields related to optoelectronics. This flexibility in applications arises from a combination of unique photo-physical properties together with the composition control to adapt properties to the specific needs. However, significant challenges in achieving long-term stability remain. To capture each step of the multi-scale degradation, from the seeds to their long-range propagation in real time, the development of *in situ* characterization techniques is essential. One core technique is transmission electron microscopy (TEM), along with peripheral analytical techniques, which allow atomic, crystallographic and mesoscale information evolution to be acquired simultaneously under external stress. By combining *in situ* live-TEM imaging, selected area electron diffraction and four-dimensional scanning TEM with automated crystal orientation mapping, we revealed the subsequent degradation steps at both nanoscopic and mesoscopic levels from inception to full degradation upon contact with water molecules. Our observations show the spinodal nature of the early-stage decomposition, where a spontaneous coexistence of CsMAFA, PbI_2 and $CsPb_2Br_5$ is observed within the same grain. When progressing, this step is followed by a dissolution/recrystallization leading to pure PbI_2 grains of two different morphologies and growth rates ($t^{1/2}$ and $t^{1/3}$), while the solid-state spinodal decomposition of CsMAFA to $CsPb_2Br_5$ continues.

[a] *Laboratoire de Réactivité et Chimie des Solides (LRCS), CNRS UMR 7314 - Institut de Chimie de Picardie FR 3085, Université de Picardie Jules Verne, 33 rue Saint Leu, FR-80039 Amiens Cedex, France. E-mail: frederic.sauvage@u-picardie.fr*
[b] *Réseau sur le stockage électrochimique de l'énergie (RS2E), CNRS FR3459 - 15 rue Baudelocque, 80039 Amiens Cedex, France*
[c] *Plateforme de Microscopie Electronique, Université de Picardie Jules Verne, Hub de l'Energie, Rue Baudelocque, 80039 Amiens Cedex, France*
[d] *EDF R&D, EDF Lab Paris-Saclay, Department SYSTEME, Palaiseau, 91120, France*
[e] *IPVF, Institut Photovoltaïque d'Ile-de-France, Palaiseau, 91120, France*

† Electronic supplementary information (ESI) available. See DOI: https://doi.org/10.1039/d4ee03381g

Introduction

The growing energy demand and the call for better exploitation of decarbonized energy sources, prompts the research towards matching the tryptic of higher performance, lower cost, and eco-friendlier photovoltaics (PV). Perovskite solar cells (PSC) are at the forefront of emerging thin film PV technologies. Since their inception with a power conversion efficiency (PCE) of 3.8% in 2009 using a liquid-junction device similar to a dye-sensitized solar cell,[1] PSCs have achieved remarkable progress, currently reaching 26.1% in a single solid-state junction and even 33.9% in tandem with crystalline silicon.[2] Such unprecedented achievements are credited to intense research in exploring the rich compositional space of hybrid halide perovskites and controlling film crystallization to obtain highly packed large particles with limited grain boundaries. Additionally, minimizing point defects through molecular passivation approaches has reduced internal non-radiative energy losses. Fundamentally, this class of materials possesses fascinating physical properties which are in all very unique, such as a tunable direct allowed transition, a long carriers diffusion length driven by low trap densities ($<10^{10}$ # cm^{-3}) and long-lived of the excited states,[3] self-healing properties and high point defects tolerance due to the high ionic character of the crystal structure and the strong antibonding coupling between Pb lone-pair s orbital and iodide p orbital.[4] The two most scrutinized compositions are the triple cation/double anion $Cs_{0.05}(MA_{0.17}FA_{0.83})_{0.95}Pb(Br_{0.17}I_{0.83})_3$ (CsMAFA)[5,6] and α-$FAPbI_3$[7–9] derivatives containing an adjustable part of methylammonium and bromide to stabilize the α-black phase. Significant efforts have been devoted to enhancing the PCE, consistently setting new records. However, stability remains a major hurdle to bring PSCs to a level comparable to crystalline silicon PV. The challenge to cope lies in addressing the severe degradation/decomposition reactions which are triggered by various external stressors including temperature, illumination, moisture, oxygen and electrical bias.

One inherent shortcoming that casts a shadow over mixed halide compositions is the halide-driven phase segregation mechanism. This reaction, triggered under light[10,11] (Hoke effect), is partially driven by the lattice entropy gain subsequently to the ions intermixing. It stems from two important factors: the hole-trapping accumulation at the iodide-site under illumination[12,13] and the long range halide mobility in the solid promoted by anionic Schottky defects (vacancies). Nevertheless, Hoke effect is a reversible near to equilibrium phenomenon. The initial atomic positions in the lattice can be recovered by placing the perovskite film back into darkness. This ionic movement, which triggers phase segregation, can be mitigated either by increasing the activation energy barrier for the iodide/bromide hopping through chloride addition,[14] decreasing the level of point defects[15–17] or through the introduction of self-assembled electron-donating ligand into the perovskite film to alleviate hole accumulation at iodide sites.[18,19] This is in contrast with the moisture-induced phase segregation, which in this case, the phase segregation is an irreversible decomposition reaction towards thermodynamically more stable by-products. In the case of $Cs_{0.05}(MA_{0.17}FA_{0.83})_{0.95}Pb(Br_{0.17}I_{0.83})_3$ under 85% R.H. exposure, the chemical decomposition leads to photo-inactive products: $CsPb_2Br_5$, PbI_2 and a Cs-poor/iodide-rich $Cs_{0.05-x}(MA_{0.17}FA_{0.83})_{0.95}Pb(Br_{0.17-2y}I_{0.83+2y})_3$ perovskite as we recently demonstrated based on *in situ* X-ray diffraction.[20,21] Improving PSC stability relies on mitigating ageing factors, such as by reducing dimensionality, introducing molecular-based passivation of surface defects, or, by applying external semi-hermetic encapsulation to shield from atmospheric species. Although these approaches have led to substantial improvement, a precise understanding of the degradation reaction and propagation pathways is essential to strategically bring PSC stability to the level of crystalline silicon (*i.e.* >25 years). Achieving stability under moisture is a paramount. Water molecules can cause a cascade of perovskite hydration in $MAPbI_3$, leading to $MAPbI_3{\cdot}H_2O$ (1D), then $MAPbI_3{\cdot}2H_2O$ (0D) or $MA_4PbI_6{\cdot}2H_2O$ (0D) which are transparent photo-inactive phases.[22,23] FA^+-based perovskites are more humidity tolerant due to their reduced dipole moment and weaker hydrogen bonding between water and FA^+.

Surveying degradation mainly relies on comparative *ex situ* analysis before and after ageing using X-ray diffraction, photoluminescence or UV-visible absorption spectroscopy.[24] This approach provides initial insights into material degradation between two end-points. However, unlike more advanced *in situ* probing techniques, *ex situ* analysis does not offer holistic information about the origin of the degradation and propagation pathways, which are crucial for understanding materials weaknesses. Additionally, removing the perovskite layer from its external stressing environment may alter the results due to the material's propensity for self-healing mechanisms. In contrast, *in situ* characterization towards *operando* conditions is beneficial for identifying the accelerating factors, thus enabling more accurate predictions of the device's lifespan.[25] *In situ* electron microscopy, for instance, has been particularly useful in elucidating heat-induced degradation pathways in $MAPbI_3$ under TEM conditions.[26,27] Light-induced degradation of $MAPbI_3$ has been reported by *in situ* scanning electron microscopy, albeit under high power wide field laser excitation (500 W cm^{-2}), revealing ion migration towards the surface and well-visible morphological change in the film.[28]

The advent of *in situ* liquid cell TEM (LC-TEM) has revolutionized the study of solid/liquid interfaces in material science.[20,29–32] This innovation enhances TEM capabilities, enabling real-time and high-resolution observations of dynamic processes within liquid solutions.[23,33–39] LC-TEM has been employed across diverse research domains, demonstrating its utility in examining nanoparticle nucleation, growth dynamics, particle movement within solutions, electrochemically mediated reactions (including deposition, corrosion, and ion transport), as well as the formation of liquid nanodroplets and bubbles.[40–52] The ability to monitor reactions in liquid medium with TEM imaging can be expanded by coupling it with advanced characterization tools such as EDX-STEM[53] for elemental mapping and 4D-STEM ACOM[54] for structural mapping based on the computation of electron diffraction pattern stacks. As the liquid flows inside the TEM cell, chemical compounds can be analyzed post-reaction by collecting the liquid and gas and using techniques like GC-MS or UV-visible techniques.[55]

In this study, novel real-time insights at atomic and mesoscale levels are provided into the moisture-induced phase segregation of CsMAFA using *in situ* liquid-cell TEM imaging. This approach is further complemented by EDX-STEM, as well as electron diffraction techniques including SAED and 4D-STEM ACOM analysis. The transformation dynamics and grain morphological changes are captured using TEM imaging and subsequently compared to theoretical models. With the help of 4D-STEM techniques in a liquid environment, we identify the degradation by-products and, based on these dynamic observations, we propose a reaction mechanism that accounts for the sequential stages inherent to the water-degradation processes occurring in CsMAFA.

Results and discussions

The CsMAFA film is deposited by spin-coating upon a specific chip based on an electron transparent Si_3N_4 window incorporated afterwards in a specifically tailors TEM sample holder (Fig. 1a–c). To adapt the film deposition to this peculiar type of substrate, we revisited and optimized the deposition conditions which are described in the experimental section. As a result, the film is composed of well-packed spherical grains of mainly *ca.* 200–300 nm and up to 500 nm without visible cracks (Fig. 1c and d). It is a relatively comparable film's morphology than that of typically encountered on conducting glass or when infiltrated into a mesoscopic layer of TiO_2. The grain boundaries are visible with less ambiguity on the TEM image (Fig. 1d), particularly on the zoomed part of the image, on which the areas of different densities between the grains are darker. Beside by X-ray diffraction, the CsMAFA phase is also confirmed using MacTempasX software that simulates the rings of an electron diffraction pattern and compared to the experimental SAED (Fig. 1e). It is clear that the film is composed of nanocrystalline particles with crystallites randomly orientated as displayed by the diffraction pattern composed of rings, corresponding to the expected CsMAFA perovskite structure as showed by the indexation and the related X-ray diffraction pattern reported in Fig. S1 (ESI†).

The reactivity of the pristine CsMAFA particles and water molecules is monitored by TEM imaging for first contact with water (Fig. 2a and b). Upon exposure to moisture, the dense CsMAFA layer collapses and leave the carbon membrane of the support visible. The curve presented in Fig. 2c shows the transparent surface zone discovered during the reaction of the perovskite over time. As shown on Fig. 2d, the quantification of the fraction of the observed transparent zone can be assessed from a simple threshold considering the light grey levels of the bare carbon membrane. This curve allows reciprocally to discuss the evolution of the surface of this zone occupied by matter, from pristine material to grains growth, and is segmented in two parts: before (blue) and after (red) 60 seconds of reaction. After 60 seconds of reaction, there is a significant change in the noise of this curve, which is attributed to different phenomena. Initially, we observed that the water took a certain time to migrate through the observed area, on these images moving from left to right, which induces a temporal shift between the reaction of the CsMAFA in different places in the image. In addition, the appearance and growth of new grains is observed during the perovskite decomposition under water reaction. The onset of this growth reaction are shifted in time and the kinetics are affected by the antagonist competitive paths between growth and dissolution. As the reaction pursues, the materials consumed for the grains growth becomes scarce. This

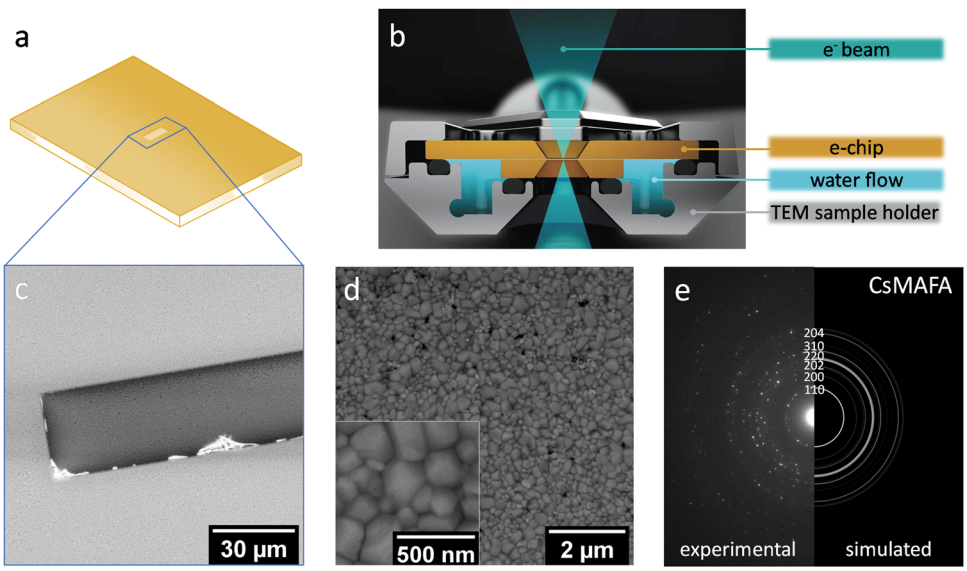

Fig. 1 (a) TEM e-chip of the protochip Poseidon select liquid cell.[56] (b) Scheme of protochip Poseidon select liquid cell composed of two chips separated by a spacer and sealed by a gasket. The gap between the chips allow liquid to pass in between in contact with the sample, and the windows of the chip allow the e-beam to pass through both the sample and the fluid. (c) and (d) SEM images of the CsMAFA sample deposited by spin-coating on the e-chip window. The size of the grains goes up to 500 nm. The particle size distribution is relatively homogeneous in the pristine. (e) Selected area electron diffraction (SAED) (left) compared to simulation with MacTempasX software of CsMAFA pristine sample and related indexation (right).

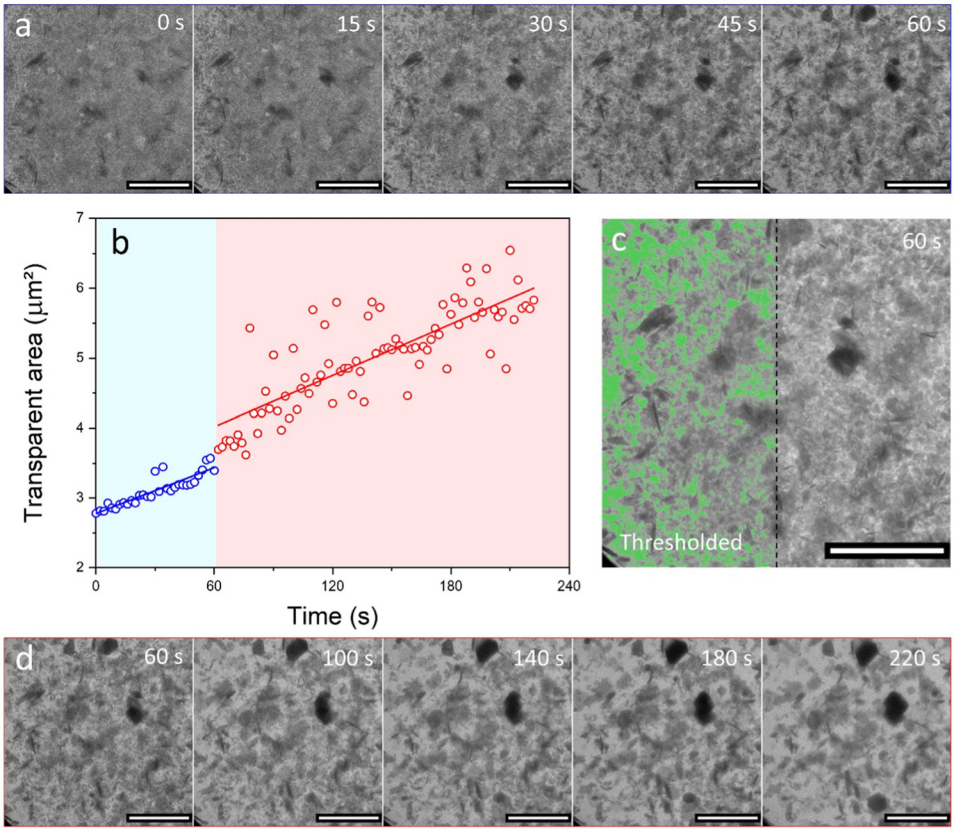

Fig. 2 Live evolution of the TEM imaging of CsMAFA reacting in contact with water molecules (a) in the first 60 s and (b) from 60 s to 220 s in water, respectively. All scale bars are 1 µm. (c) Growth of the transparent area of the image while CsMAFA in contact with water. The first sequence (blue) started few seconds after the micro-injection of water molecules in the cell and ended when big particles started to grow at around 60 s. The second sequence (red) contains much more noise due to non-simultaneous expansions and coalescences of several particles along with the 2D projection of the image. (d) Raw image (right) and threshold applied on it (left) to select the brightest part of the image map the regions of liquid only called transparent area in this work.

modifies this competition and notably increases the diversity of grain sizes. This explains the noise level increase in the evolution of the area occupied by matter over time. To resume, the partial dissolution of the perovskite layer is accompanied by a non-homogeneous increase in the concentration of growth nuclei. The induced non-simultaneous growth of the new grains and their proximity led to competitive phenomena between growth and particles coalescence triggered by surface energy minimization as shown in Fig. 2.

In order to grasp further information on the new particles formed at the end of the water-induced perovskite degradation, the STEM images presented in Fig. 3 show that the main morphologies observed are either hexagonal-shaped (a) and (c) or needle-shaped (d) and (e) particles. The corresponding EDX cartographies highlight the presence of Pb, Cs and I, and the SAED (g) and (i) confirms the presence of PbI_2 and $CsPb_2Br_5$ structures among those grains. These electron diffraction images were acquired on individual grains of various morphologies present outside of the circled region of interest (ROI) shown in Fig. 3h. The needle-like particles are attributed to PbI_2 and the hexagonal shaped particles mainly to $CsPb_2Br_5$, however with a potential coexistence of PbI_2 within the same grain as showed by the EDX analysis and based on 4D-STEM analysis presented in the following. These two by-products were observed in previous work from our group led by *in situ* X-ray diffraction and solid-state 2D NMR under 85% R.H.[20] This observation supports that between 80–85% R.H. condition and pure water as herein in this study, the reaction pathways are same and only the kinetic of the perovskite decomposition differs. The thickness of $CsPb_2Br_5$ grains is comparable to those of PbI_2 due to the relative homogeneity of the resulting grain size between the two morphologies. The halo around the central spot of the images (Fig. 3g and i) stems from the diffusion of the parallel electron beam through the liquid and the grains.

If we further analyze the grain growth, the TEM image sequences presented in Fig. 4 show the growth of three individual particles (a)–(c). As the microfluidic flow of water in the protochip cell is relatively low, we were able to observe the sluggish water progression in contact with the perovskite. On other words, it is then possible to monitor the progression of the perovskite degradation in various regions of interest to multiply the measurements. The liquid depth in the cell between the perovskite layer and the upper window led to electron beam scattering phenomena. This generates noise during the imaging capture in conventional TEM experiments as aforementioned. However, in order to limit the apparent

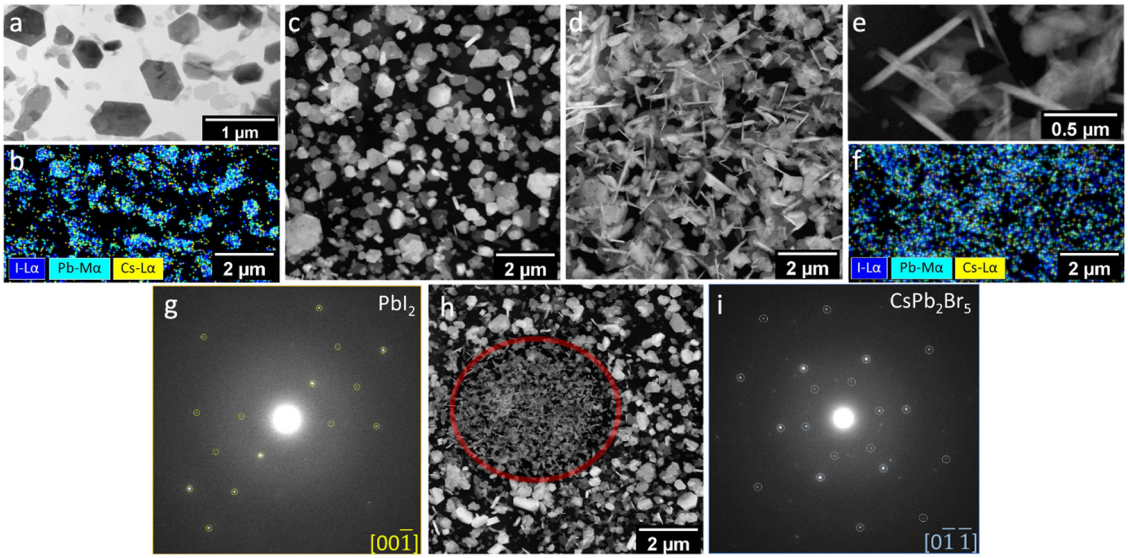

Fig. 3 (a) and (c) Scanning transmission electron microscopy (STEM) of an area showing mostly hexagonal-shaped $CsPb_2Br_5$-based particles and (b) corresponding electron dispersive X-ray spectroscopy (EDX). (d) and (e) STEM of mainly needle-shaped PbI_2 particles and (f) corresponding EDX. Those particles of different morphologies and sizes are both visible in the STEM image (h) drifting in the water and forming quasi-isomorphic regions as the "needle nest" circled in red. (g) and (i) Selected area electron diffraction (SAED) of PbI_2 and $CsPb_2Br_5$. After 20 minutes in water, several "well-shaped" PbI_2 particles appeared and reached their maximum size. Crystal phases and orientations are identified using ASTAR.

noise and facilitate the segmentation of the individual grains, the images of the *in situ* videos were summed and normalized in gray level per packet of 50 consecutive images, as described in Fig. 4d. The corresponding segmented images are superposed to follow the evolution of the morphologies in real-time. The Fig. 4e shows by comparison that the growth of "well-shaped" grains is in a multi-stage evolution, which corresponds to expansion phases projected onto a plane normal to the *Z*-axis of the microscope.

For $CsPb_2Br_5$ particles, in addition to the nucleation and growth, we can see the coalescence of two self-similar particles, namely 1a and 1b. The nucleation points were sufficiently close to form particle 1 after less than 60 seconds of contact with water molecules. The driving force for this fusion between two nanoparticles stems from thermodynamic consideration where the surface energy of the primary nanoparticles is minimized through such a mechanism which is herein captured in real-time thanks to this *in situ* TEM approach.[57–59] This driving force becomes unlikely with increasing nanoparticle size.[60]

The growth of the byproducts resulting from the perovskite degradation exhibits two different rates depending on time, which affect overall the final particles morphology. Nucleation and growth are processes qualitatively well described by the classical theory of nucleation (CNT)[61,62] and the coarsening model of Lifshitz–Slyozov–Wagner (LSW), respectively.[63–65] For the nanocrystals coarsening, the LSW model predicts two asymptotic limits: diffusion and reaction-limited growth. As shown in Fig. 4f, the growth of the three represented grains follow variable trends as a function of time. The growth curve of particle 3, corresponding to PbI_2, follows at first a law in $t^{1/3}$ which is attributed to a reaction-limited process as it is described in the LSW model, although not all initial assumptions of the LSW model such as the spherical morphology of the particles, the constant diffusion coefficient in the media or a single nanocrystal in a free solution are herein verified. For longer time, the growth rate changes to a law in $t^{1/2}$ which corresponds to a diffusion-limited process for the ripening mechanism of the PbI_2 particles growth in which diffusion limitation is driven by a concentration decrease of lead and iodide in the interphase solution. This view of competitive dynamic between the different particle's growth, affected by their related packing, explains the variations in grain growth regimes over time. Towards the end of its growth, both particles 2 and 3 follow a law in a $t^{1/2}$ power law, consistent with what is predicted for a diffusion-controlled particles growth.

The 4D-STEM[66] approach has been deployed to map the phases and crystalline orientations of CsMAFA in the pristine state as shown in Fig. S2 (ESI†) and then during its moisture-induced degradation (Fig. 5). These maps are obtained by pattern matching, as each diffraction pattern is compared to a bank of diffraction patterns generated for each orientation of each searched crystalline structure. These phase maps are controlled by reliability maps that reveal the degrees of reliability between the determined phases and the other phases as input. Likewise, the reliability orientation maps compare the determined orientation with the other possible orientations of all the input phases. In the end, these reliability maps represent a map of confidence factors for each phase and each orientation determined by 4D-STEM.

In agreement with the other measurements of this work, particularly the STEM and EDX maps, we observe the presence of a majority of PbI_2 grains after the first contact of CsMAFA with water. The signal-to-noise ratio of the diffraction images is affected by the thickness of the grains which scatters the electrons, as it can be seen on the diffraction images of Fig. 5

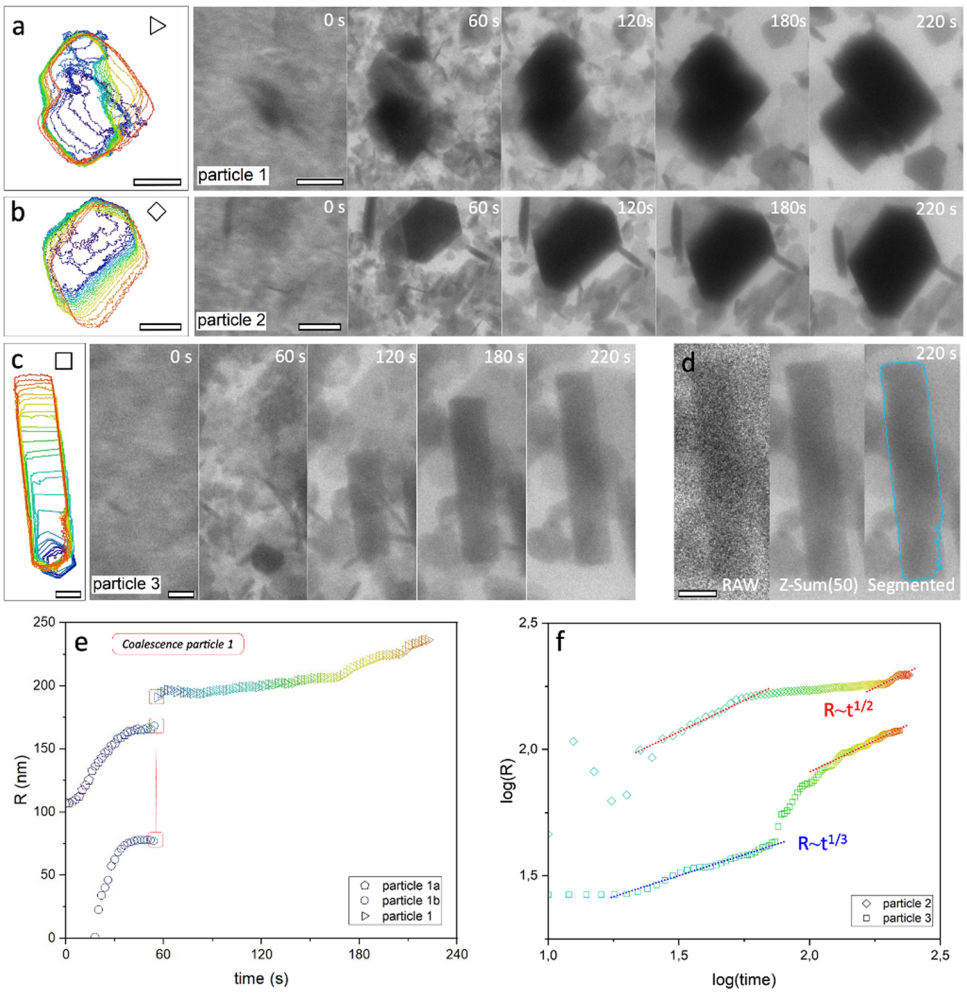

Fig. 4 (a)–(c) Growth of well-shaped particles in water tracked by TEM. The particles grow in water and reach different sizes up to about 500 nm, depending on their largest dimension. The TEM images were segmented with the WEKA segmentation 3D plugin in ImageJ corresponding to the particles presented in a–c. Each color refers to a specific time. All scale bars are 200 nm. (d) From left to right: Raw image as captured by the camera, *Z*-sum of its 50 neighbors in the stack, the outline of the particle area obtained by segmentation. (e) The evolution of the normalized radius of the particle 1 by the time of water contact. Particles 1a and 1b coalescences are indicated. The radius is normalized as the radius of a disk of the same surface as the particle. (f) Comparison of particle 2 and particle 3 growth with LSW power laws. The TEM images are summed and normalized along the *Z*-axis of the image stack to increase the signal/noise ratio. The color code is the same on the segmented images and the graph.

corresponding to grains of various thicknesses. At the scale of the same observation zone of a few microns, it can be considered that the thickness of the liquid is homogeneous and that it has a much less pronounced impact than the thickness of the grains on the diffusion of the electron beam and thus on the information quality contained in the diffraction images. The reliability maps (reported in Fig. 5c and f) give indications on the influence of the grain thickness on the possibility of taking the points into account for the analysis. Indeed, the reliability tends to strongly decrease with the thickness of the grains, because the phenomena of diffusion decrease the quality of the signal in the diffraction shots. During the pattern-matching process, the correspondence between the reference pattern and a noisy diffraction pattern results in a low index score with too little contrast depending on the templates to give a high reliability value to the one that best matches. The superimposition of different relatively fine grains in the observation area leads to diffraction image constructions that combine several crystallographic structures or orientations of the same structure. Reliability maps are herein used to determine the predominant structure in a shot and thus to ascertain on the degree of certainty given to the phase and orientation of the grains. Note also that the difference between the space groups, and therefore, the diffraction images expected for each phase ($CsPb_2Br_5$ and PbI_2) effectively dispel the doubts about the determination of the phases as well as of the crystallographic orientations. Interestingly, the 4D-STEM analysis highlights the complexity of the water-induced phase segregation process at nanoscale. Going beyond the aforementioned dissolution/recrystallization process, within a grain analysis, we can find multiple spinodal regions showing the coexistence of either the two by-products $CsPb_2Br_5$ and PbI_2 or even the original perovskite structure with these latter (Fig. 5b and e). This means that perovskite particles before

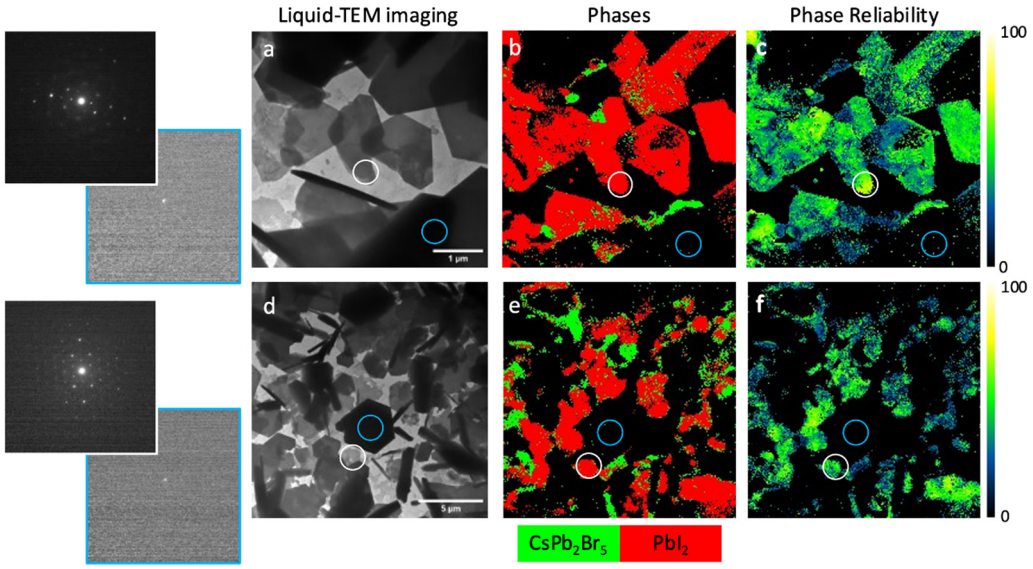

Fig. 5 (a) and (d) TEM-liquid imaging and (b) and (e) 4D-STEM ASTAR crystalline phase maps of particles in liquid. (c) and (f) The associated phase reliability maps the degree of confidence linked to phase maps and are calculated as a function of the numbered indexed spots by pattern matching. The phases maps (b) and (e) combine the phase, indexation, and reliability maps with a minimum reliability of 5. The diffraction patterns present in the figure are taken directly from the 4D-STEM dataset and refer to regions of fine/thick grains indicated on the maps by circles.

the process of dissolution/recrystallization, become spontaneously thermodynamically unstable at nanoscale in contact with water molecules, thus supporting the spinodal decomposition mechanism between CsMAFA, $CsPb_2Br_5$ and PbI_2. We estimate that such a spinodal decomposition, which stems from the direct contact between the perovskite and the water molecules, will also take place in lower concentration of water molecules, at least with a relative humidity down to 80–85%.

For longer exposure time to water, some well-shaped particles start to disentangle after 80 minutes in water as showed in Fig. 6. These particles drift under the microfluidic water flow. Some other particles remain aggregated in certain areas and the SAED made after 80 minutes exposure to water shows the sole presence of PbI_2, whereas the $CsPb_2Br_5$ has been dissolved into the medium upon time. As shown in Fig. 6, some crystals are well isolated from the original fragmented grains, and some nanocrystals remain aggregated in packets forming clusters of several microns. These observations of the water-induced degradation of CsMAFA show similarities with the in-air degradation of the $MAPbI_3$ described by A. Alberti *et al.*[21] as the

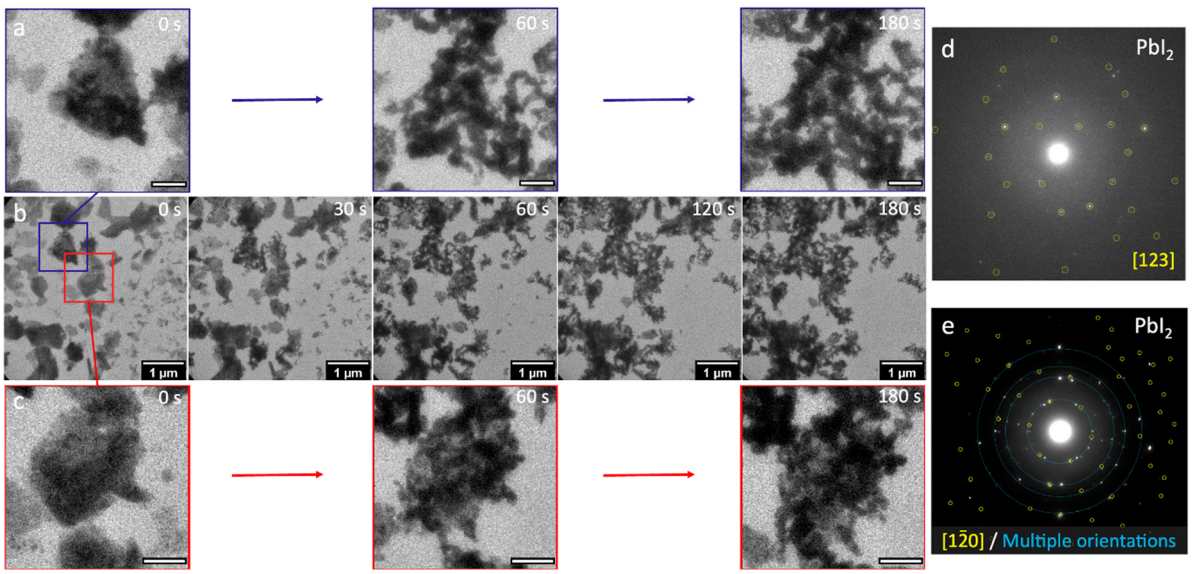

Fig. 6 (b) TEM monitoring of particles of PbI_2 at the end of the experiment (scale bars are 1 µm). (a) and (c) higher magnification of zone showed in (b) (scale bars are 250 nm). The crystals lose their geometrical shape and split into several crystalline pieces that drift in the water. (d) SAED made after the degradation of the well-shaped crystals have only shown the presence of PbI_2. (e) SAED of PbI_2 nanocrystals with one orientation identified [1–20] and several rings indicating the presence of multiple crystals with different orientations. Crystal phases and orientations are found using 4D-STEM ACOM.

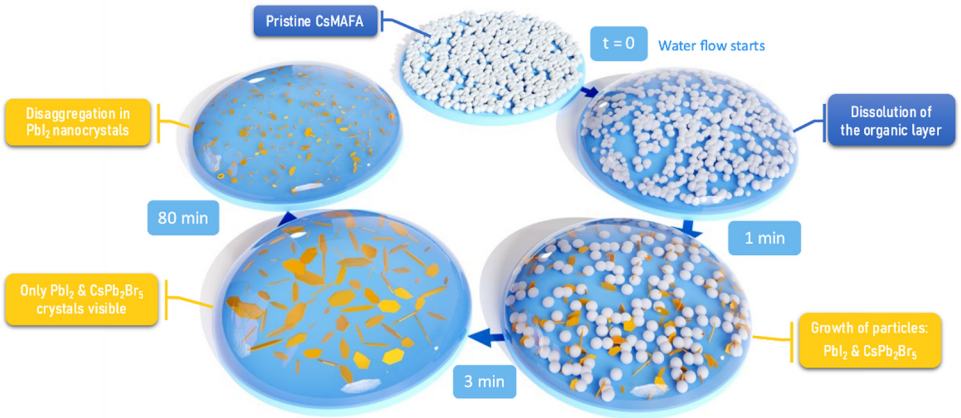

Fig. 7 Synthesis of observations and reaction scheme of CsMAFA in water monitored by TEM techniques. At time t = 0, the water meets the pristine material. Until approximately t = 60 s of reaction, the organic layer is dissolved and spinodal regions in grain are formed showing the co-existence of CsMAFA, PbI_2 and $CsPb_2Br_5$ as deduced from 4D-STEM ASTAR. Further grains growth takes place by dissolution/recrystallization. The largest particles size is attained at t = 180 s. The 4D-STEM-ASTAR maps show grains of PbI_2 and $CsPb_2Br_5$ surrounded by liquid, with a very predominant proportion of PbI_2 grain. Finally, the grains formed disintegrate and drift in the liquid, and remain in this state until the end of the observations at t = 80 min.

transformation of the $MAPbI_3$ core to fragmented and interconnected nano-grains of 6H-PbI_2. Fig. 7 schematizes the overall degradation pathways for CsMAFA perovskite under water on the basis of this *in situ* TEM investigation. To resume, the degradation takes place into mainly three key steps, namely (i) spontaneous spinodal decomposition of the perovskite particles at nanoscale into PbI_2 and $CsPb_2Br_5$ with dissolution of the organic layer, (ii) dissolution/recrystallization processes leading to PbI_2 and $CsPb_2Br_5$ leading to complete degradation of the perovskite and (iii) overall disaggregation of PbI_2 nanocrystals.

Conclusions

In conclusion, by combining complementary analysis techniques (*i.e.* 4D-STEM, EDX mapping and ASTAR) with live TEM imaging, we have revealed, for the first-time, live information at both the nano and mesoscale about the decomposition mechanisms of CsMAFA in contact with water. The phase and orientation maps acquired in 4D-STEM ASTAR, complemented by elemental EDX maps, highlighted the spontaneous nanoscale formation of spinodal regions in perovskite grain, specifically between CsMAFA, PbI_2 and $CsPb_2Br_5$. This spinodal decomposition either competes with or is followed by a dissolution/recrystallization mechanism from CsMAFA to PbI_2. The segmentation of TEM images shows different growth laws controlling the final grain morphology. This morphology is influenced by the immediate vicinity of the particles, as described by the LSW model, with variations in Pb^{2+} and I- concentrations controlling diffusion and particle/particle interactions in the liquid, significantly affecting the growth of neighboring PbI_2 grains. The results presented in this work underline the heterogenous complexity of the degradation mechanisms of CsMAFA perovskite when exposed to water molecules. Understanding these complex reactivities through *in situ* advanced characterization techniques is paramount for better apprehending the multiscale degradation mechanisms of perovskites, thereby aiding in the development of more robust perovskite compositions against humidity-induced external stressors.

Experimental section

TEM instrument

The *in situ* degradation of the CsMAFA sample in contact with water was followed using a FEI Tecnai F20 HRTEM (200 keV) equipped with a Gatan OneView CMOS camera and ASTAR NanoMegas system with electron beam precession.

Camera

The evolution of the sample in time was followed by TEM imaging with a Gatan OneView CMOS camera. This camera's high spatial resolution and sensibility allowed video sequences to be recorded in 4K with an exposition of 20 ms to 40 ms per image, corresponding to rates of 25 to 50 images acquisition per second. This sensibility also allows collecting selected area electron diffraction with a good intensity resolution in 4K images with 32 bits for grey levels. The TEM images reported in the manuscript are recorded using a low electron dose rate in order to avoid any possible effects from the electronic beam probe. The dose received by the perovskite sample is from 0.1 to 2.4 e^- $Å^{-2}$ s^{-1}.[8] This latter has been precisely quantified using GMS3 DigitalMicrograph® software.

Perovskite on microchip fabrication

CsMAFA film was spin-coated onto an E-chip (Protochips) equipped with an electron transparent amorphous silicon nitride (Si_3N_4) window with a thickness of 30 nm. For the film's preparation, we used a concentration of 0.5 mol L^{-1} precursor solution within an Ar-filled glovebox; first at 3000 rpm for 10 seconds and then 6000 rpm for 20 seconds. During the second step, 100 µL of chlorobenzene as an anti-solvent was dropped 10 seconds before the end of the program. The E-chip was post-

annealed at 110 °C for 30 minutes inside the glovebox leading to a film thickness of ~200 nm.

Liquid cell TEM

Under a binocular optical microscope, the liquid cell is mounted into the TEM holder in a sandwich configuration with a sample top chip and a spacer bottom chip. Both chips are in contact with a two levels O-ring gasket to ensure good sealing. The spacer chip fixes a gap of 1 μm for the water flow. The lid of the TEM sample holder is screwed on top with a clamping force fixed by a torque screwdriver. The sealing is then tested before the insertion in the TEM with a turbopump (10^{-9} Torr). For this, we ensured that the pressure value remains constant while the sample holder is inserted and kept under a vacuum in the pumping station. Then, the plugs of the internal fluidic tubing circuit (inlets and outlets) are unscrewed one after the other to check that there is no pressure variation. After 20 minutes of this sealing test, all plugs are placed back. The specimen holder is then inserted into the TEM, the plugs of the inlet and outlet are removed. The inlet is connected *via* a PEEK tubing set to a 5 mL syringe filled with water mounted on a pump, and the outlet is connected to a vial equipped with a septum so that the whole circuit is sealed. The thickness of the liquid in the cell depends on the spacer that fixes a gap of 1 μm between the chip. However, note that because the difference of pressure between the liquid within the cell (1 atm) and the vacuum in the column of the TEM (10^{-9} Torr), the window bends slightly outward, increasing the gap between the chips, especially in the middle of the window.[3]

4D-STEM ACOM

The ASTAR-Nanomegas system is used for automatic TEM phase-orientation mapping with a precession diffraction frequency of 100 Hz. The sample electron diffraction patterns were acquired with an accelerated electron voltage of 200 kV and operating with a precession angle of 0.7 degree. The scan sizes are from 100 × 100 pixels to 200 × 200 pixels. The precession is piloted with Digistar software of the ASTAR system, provided by Nanomegas. The scan of diffraction patterns is acquired with a CMOS Oneview Camera, which has been prior realigned with the ASTAR software. The identification of phases was made by pattern matching using CIF files of the expected pristine and products of reaction with water.

Liquid injection

Prior to the liquid injection, the pristine CsMAFA layer was characterized by TEM, STEM-HAADF imaging and EDX-STEM spectroscopy. A flow rate of 5 μL min^{-1} was maintained by the pump after the different characterization tools herein used for the pristine material. The arrival of water in the cell was monitored by TEM imaging. It takes several minutes for the water to come to the cell from the syringe through the 50 cm length of the tubing.

Liquid *in situ* characterization techniques

At first contact of CsMAFA with water, a video sequence was recorded and is presented in Fig. 2. We observed first growth of the transparent area of the image, then the formation of well-shaped particles as with different morphologies as hexagonal PbI_2 described by Fu *et al.*[9] TEM monitoring shows that these particles formed in a few minutes in the water and then slowly drifted into the liquid. Groups of particles were characterized by EDX and STEM, and SAED shows the presence of $CsPb_2Br_5$ and PbI_2. After 80 minutes in water, we observed by TEM imaging that the particles lost their shapes and decomposed in several pieces drifting in the liquid. From this point, electron diffractions on the remaining particles showed the presence of only PbI_2. EDX cartography is made with Esprit2.0 software.

Image treatment

The growth study of single particles upon CsMAFA degradation in water was analysed using the WEKA random-forest segmentation 3D plugin of the software ImageJ. As shown in Fig. 3, the growth is followed by taking into account the area covered by the projection of the particle on a 2D image fitted to a disk to compare different particle growths with their normalized R radius. The identification of diffraction patterns was proceeded using ASTAR Nanomegas and MacTempaX software.

Author contributions

M. A. A. K. optimized the perovskite deposition procedure upon Si_3N_4 e-chips and designed specific chips by 3D printing for enabling spin-coating on the e-chips. F. S. programmed this research within the group of perovskite and established the collaboration with A. D. F. S. and A. D. designed the experiments, supervised the overall work, manuscript writing and obtained financial supports. K. C. and N. F. carried out the 4D-STEM analyses. J. R. participates to the financial support of M. A. A. K. and to the discussions of this work. A. J. assisted in sample preparation and performing scanning and transmission electron microscopy.

Data availability

The data supporting this article have been included as part of the ESI.† The live data related to *in situ* TEM will be available upon request from the authors (>1 Gb).

Conflicts of interest

The authors declare no competing interests.

Acknowledgements

M. A. A. K. is indebted to the financial support of region Hauts-de-France and Electricité de France (EDF). F. S. acknowledges financial support of the latter, the Agence Nationale de la Recherche under the France 2030 program, MINOTAURE project, Grant # ANR-22-PETA-0015, Horizon Europe ''LAPERITIVO'' project under the grant agreement number 101147311 and the ERC AdG ''GEMINI''. A. D. thanks the Agence Nationale

de la Recherche for funding the project DestiNa-ion *Operando* under grant agreement ANR-19-CE42-0014.

References

1 A. Kojima, K. Teshima, Y. Shirai and T. Miyasaka, *J. Am. Chem. Soc.*, 2009, **131**, 6050–6051.
2 Best-research-cell-efficiencies.20200104-annotated.pdf.
3 M. A. Green, A. Ho-Baillie and H. J. Snaith, *Nat. Photonics*, 2014, **8**, 506–514.
4 W. J. Yin, T. Shi and Y. Yan, *Appl. Phys. Lett.*, 2014, **104**, 063903.
5 H. Oga, A. Saeki, Y. Ogomi, S. Hayase and S. Seki, *J. Am. Chem. Soc.*, 2014, **136**, 13818–13825.
6 J.-P. Correa-Baena, M. Saliba, T. Buonassisi, A. Abate, W. Tress and A. Hagfledt, *Science*, 2017, **358**(80), 739–744.
7 G. E. Eperon, S. D. Stranks, C. Menelaou, M. B. Johnston, L. M. Herz and H. Snaith, *Energy Environ. Sci.*, 2014, **7**, 982–988.
8 N. J. Jeon, J. H. Noh, W. S. Yang, Y. C. Kim, S. Ryu, J. Seo and S. I. Seok, *Nature*, 2015, **517**, 476–480.
9 H. Lu, Y. Liu, P. Ahlawat, A. Mishra, W. R. Tress, F. T. Eickemeyer, Y. Yang, F. Fu, R. Wang, C. E. Avalos, B. I. Carlsen, A. Agarwalla, X. Zhang, X. Li, Y. Zhan, S. M. Zakeeruddin, L. Emsley, U. Rothlisberger, L. Zheng, A. Hagfeldt and M. Grätzel, *Science*, 2020, **370**, 74.
10 E. T. Hoke, D. J. Slotcavage, E. R. Dohner, A. R. Bowring, H. I. Karunadasa and M. D. McGehee, *Chem. Sci.*, 2015, **6**, 613–617.
11 D. J. Slotcavage, H. I. Karunadasa and M. D. McGehee, *ACS Energy Lett.*, 2016, **1**, 1199–1205.
12 J. T. Dubose and P. V. Kamat, *J. Am. Chem. Soc.*, 2020, **142**, 5362–5370.
13 G. F. Samu, A. Balog, F. De Angelis, D. Meggiolaro, P. V. Kamat and C. Janaky, *J. Am. Chem. Soc.*, 2019, **141**, 10812–10820.
14 J. Cho and P. V. Kamat, *Chem. Mater.*, 2020, **32**, 6206–6212.
15 S. Draguta, O. Sharia, S. J. Yoon, M. C. Brennan, Y. V. Morozov, J. S. Manser, P. V. Kamat, W. F. Schneider and M. Kuno, *Nat. Commun.*, 2017, **8**, 200.
16 S. J. Yoon, M. Kuno and P. V. Kamat, *ACS Energy Lett.*, 2017, **2**(7), 1507–1514.
17 M. C. Brennan, S. Draguta, P. V. Kamat and M. Kuno, *ACS Energy Lett.*, 2018, **3**(1), 204–213.
18 R. A. Belisle, K. A. Bush, L. Bertoluzzi, A. Gold-Parker, M. F. Toney and M. D. McGehee, *ACS Energy Lett.*, 2018, **3**(11), 2694–2700.
19 A. J. Knight, A. D. Wright, J. B. Patel, D. P. McMeekin, H. Snaith, M. B. Johnston and L. M. Herz, *ACS Energy Lett.*, 2019, **4**, 75–84.
20 M. A. Akhavan Kazemi, N. Folastre, P. Raval, M. Sliwa, J. M. V. Nsanzimana, S. Golonu, A. Demortiere, J. Rousset, O. Lafon, L. Delevoye, G. N. Manjunatha Reddy and F. Sauvage, *Energy Environ. Mater.*, 2023, **6**, e12335.
21 A. Alberti, C. Bongiorno, E. Smecca, I. Deretzis, A. La Mamgna and C. Spinella, *Nat. Commun.*, 2019, **10**, 2196.
22 J. A. Christians, P. A. Miranda Herrera and P. V. Kamat, *J. Am. Chem. Soc.*, 2015, **137**(4), 1530–1538.
23 M. A. Akhavan Kazemi, P. Raval, K. Cherednichekno, J. N. Chotard, A. Krishna, A. Demortiere, G. N. Manjunatha Reddy and F. Sauvage, *Small Methods*, 2021, **5**, 2000834.
24 J. Hidalgo, C. A. R. Perini, A. F. Castro-Mendez, D. Jones, H. Köbler, B. Lai, R. Li, S. Sun, A. Abate and J. P. Correa-Baena, *ACS Energy Lett.*, 2020, **5**(11), 3526–3534.
25 E. Smecca, Y. Numata, I. Deretzis, G. Pellegrino, S. Boninelli, T. Miyasaka, A. La Magna and A. Alberti, *Phys. Chem. Chem. Phys.*, 2016, **18**, 13413–13422.
26 G. Divitini, S. Cacovich, F. Matteocci, L. Cina, A. Di Carlo and C. Ducati, *Nat. Energy*, 2016, **1**, 15012.
27 B. Yang, O. Dyck, W. Ming, M. H. Du, S. Das, C. M. Rouleau, G. Duscher, D. B. Geohegan and K. Xiao, *ACS Appl. Mater. Interfaces*, 2016, **8**, 32333–32340.
28 H. Yuan, E. Debroye, K. Janssen, H. Naiki, C. Steuwe, G. Lu, M. Moris, E. Orgiu, H. Uji-i, M. De Schryver, P. Samori, J. Hofkens and M. Roeffaers, *J. Phys. Chem. Lett.*, 2016, **7**, 561–566.
29 H. Zheng, R. K. Smith, Y. W. Jun, C. Kisielowski, U. Dahmen and P. Alivisatos, *Science*, 2009, **324**(5932), 1309–1312.
30 S. Pu, C. Gong and A. W. Robertson, *R. Soc. Open Sci.*, 2020, **7**, 191204.
31 A. R. Harutyunyan, G. Chen, T. M. Paronyan, E. M. Pigos, O. A. Kuznetsov, K. Hewaparakrama, S. M. Kim, D. Zakharov, E. A. Stach and G. U. Sumanasekera, *Science*, 2009, **326**(5949), 116–120.
32 B. J. Kim, J. Tersoff, S. Kodambaka, M. C. Reuter, E. A. Stach and F. M. Ross, *Science*, 2008, **322**(5904), 1070–1073.
33 M. J. Williamson, R. M. Tromp, P. M. Vereecken, R. Hull and F. M. Ross, *Nat. Mater.*, 2003, **2**, 532–536.
34 H. G. Liao and H. Zheng, *Annu. Rev. Phys. Chem.*, 2016, **67**, 719–747.
35 C. Wang, X. Chen, Y. Wu, Y. Li and S. Cheng, *J. Phys. Chem. C*, 2020, **124**, 26018–26025.
36 H. G. Liao, L. Cui, S. Whitelam and H. Zheng, *Science*, 2012, **336**(6084), 1011–1014.
37 J. E. Evans, K. L. Jungjohann, N. D. Browning and I. Arslan, *Nano Lett.*, 2011, **11**, 2809–2813.
38 H. Zheng, S. A. Claridge, A. M. Minor, A. P. Alivisatos and U. Dahmen, *Nano Lett.*, 2009, **9**, 2460–2465.
39 E. R. White, S. B. Singer, V. Augustyn, W. A. Hubbard, M. Mecklenburg, B. Dunn and B. C. Regan, *ACS Nano*, 2012, **6**, 6308–6317.
40 M. Gu, L. R. Parent, B. M. Mehdi, R. R. Unocic, T. McDowell, R. L. Sacci, W. Xu, J. G. Connell, P. Xu, P. Abellan, X. Chen, Y. Zhang, D. E. Perea, J. E. Evans, L. J. Lauhon, J. G. Zhang, J. Liu, N. D. Browning, Y. Cui, I. Arslan and C. M. Wang, *Nano Lett.*, 2013, **13**, 6106–6112.
41 X. Chen, K. W. Noh, J. G. Wen and S. J. Dillon, *Acta Mater.*, 2012, **60**, 192–198.
42 U. Mirsaidov, C. D. Ohl and P. A. Matsudaira, *Soft Matter*, 2012, **8**, 7108–7111.
43 E. R. White, M. Mecklenburg, S. B. Singer, S. Aloni and B. C. Regan, *Appl. Phys. Express*, 2011, **4**(5), 55201.

44 D. Li, M. H. Nielsen, J. R. I. Lee, C. Frandsen, J. F. Banfield and J. J. De Yoreo, *Science*, 2012, **336**, 1014–1018.
45 T. W. Huang, S. Y. Liu, Y. J. Chuang, H. Y. Hsieh, C. Y. Tsai, W. J. Wu, C. T. Tsai, U. Mirsaidov, P. Matsudaira, C. S. Chang, F. G. Tseng and F. R. Chen, *Soft Matter*, 2013, **9**, 8856.
46 M. T. Proetto, A. M. Rush, M. P. Chien, A. Baeza, J. P. Patterson, M. P. Thompson, N. H. Olson, C. E. Moore, A. L. Rheingold, C. Andolina, J. Millstone, S. B. Howell, N. D. Browning, J. E. Evans and N. C. Gianneschi, *J. Am. Chem. Soc.*, 2014, **136**, 1162–1165.
47 N. D. Jonge, D. B. Peckys, G. J. Kremers and D. W. Piston, *Proc. Natl. Acad. Sci. U. S. A.*, 2009, **106**, 2159–2164.
48 U. M. Mirsaidov, H. Zheng, Y. Casana and P. Matsudaira, *Biophys. J.*, 2012, **102**, L15–L17.
49 J. E. Evans, L. Jungjohann, P. C. K. Wong, P. L. Chiu, G. H. Dutrow, I. Arslan and N. D. Browning, *Micron*, 2012, **43**, 1085–1090.
50 B. Luo, J. W. Smith, Z. Ou and Q. Chen, *Acc. Chem. Res.*, 2017, **50**, 1125–1133.
51 K. H. Nagamanasa, H. Wang and S. Granick, *Adv. Mater.*, 2017, **29**, 1703555.
52 X. Chen, C. Li and H. Cao, *Nanoscale*, 2015, **7**, 4811–4819.
53 L. Lutz, W. Dachraoui, A. Demortière, L. R. Johnson, P. G. Bruce, A. Grimaud and J.-M. Tarascon, *Nano Lett.*, 2018, **2**, 1280–1289.
54 A. Gomez-Perez, A. Galanis, P. Das, S. Nicolopoulos and A. Demortière, *Microsc. Microanal.*, 2021, **27**(S1), 2234–2235.
55 K. G. Moncayo, N. Folastre, M. Toledo, H. Tonnoir, F. Rabuel, G. Gachot, D. Huo and A. Demortière, *Small Methods*, 2024, 2400365.
56 *Protochips Micros. Today*, 2017, **25**, 13.
57 M. R. Zachariah and M. J. Carrier, *J. Aerosol Sci.*, 1999, **30**, 1139–1151.
58 K. E. J. Lehtinen and M. R. Zachariah, *J. Aerosol Sci.*, 2002, **33**, 357–368.
59 K. E. J. Lehtinen and M. R. Zachariah, *Phys. Rev. B: Condens. Matter Mater. Phys.*, 2001, **63**, 205402.
60 M. José-Yacamán, C. Gutierrez-Wing, M. Miki, D. Q. Yang, K. N. Piyakis and E. Sacher, *J. Phys. Chem. B*, 2005, **109**, 9703–9711.
61 G. S. Redner, C. G. Wagner, A. Baskaran and M. F. Hagan, *Phys. Rev. Lett.*, 2016, **117**, 1–7.
62 X. M. Bai and M. Li, *J. Chem. Phys.*, 2006, **124**, 124707.
63 I. M. Lifshitz and V. V. Slyozov, *J. Phys. Chem. Solids*, 1961, **19**, 35–50.
64 N. T. K. Thanh, N. Maclean and S. Mahiddine, *Chem. Rev.*, 2014, **114**, 7610–7630.
65 U. Simon, *Angew. Chem.*, 2008, **47**(12), 2174–2175.
66 E. F. Rauch, M. Veron, S. Nicolopoulos and D. Bultreys, *Solid State Phenom.*, 2012, **186**, 13–15.